Journal of Theoretical and Applied Information Technology
30th April 2022. Vol.100. No 8

ISSN: 1992-8645 www.jatit.org E-ISSN: 1817-3195

SPECTRAL UNMIXING OF HYPERSPECTRAL IMAGES USING MULTI-OBJECTIVE LION-RIDER OPTIMIZATION TECHNIQUE

[1] RAJA NATARAJAN, [2] VADIVEL RAMASAMY
[1]Ph.D. Scholar, Department of Information Technology, Bharathiar University, Coimbatore, India
Assistant Professor (Computer Science), Tamil Nadu Agricultural University, Coimbatore, India
[2]Assistant Professor, Department of Information Technology, Bharathiar University, Coimbatore,
E-mail: [1]nraja@tnau.ac.in, [2]vlr_vadivel@yahoo.co.in

ABSTRACT

In hyperspectral image processing, spectral unmixing is a key computation for extracting endmembers and determining their fractional abundances from mixed pixels. Despite the fact that the sparse unmixing model has recently attracted a lot of attention, the acquired hyperspectral images are influenced by noise, indicating that the sparse unmixing model needs to be improved in order to extract the best collection of endmembers. The Lion-Rider algorithm is proposed in conjunction with a linear sparse spectral unmixing to address this complexity. The proposed optimization algorithm determines the fractional abundances of the endmembers bydefining a multi-objective function. The objective function includes Euclidean and Frobenius norms and optimization variables that are associated with the abundance and mixing matrices. The proposed lion-rider optimization approach is the modified rider optimization algorithm whichuses lion optimization algorithm as anintegral component of computation.To define the objective function in estimating fractional abundances, the optimization variables namely Reconstruction Error, Sparsity, Spatial Neighbor, and Spatial Neighbor Correlation are used simultaneously. Urban and Cuprite hyperspectral image datasets are used to evaluate the proposed method. Based on the performance analysis, the proposed lion-rider optimization approach outperformed its competitors namely,Bilinear and Trilinear Multi-Objective Spectral Unmixing, Robust Collaborative Nonnegative Matrix Factorization, Pareto-Multi-Objective Spectral Unmixing, and Rider Optimization, in estimating the endmembers and their correspoinding fractional abundances with a minimal reconstruction error and root mean square error of 22.4027 and 0. 0297, respectively.

Keywords: *Hyperspectral Image; Spectral Unmixing; Endmembers; Fractional Abundance; Multi-Objective Function.*

1. INTRODUCTION

Hyperspectral Image (HSI) processing technology is gaining momentum in recent years as the airborne and spaceborne sensors have enhanced the ground based data collection practices in various application domains(Bioucas-Dias et al., 2012). Using the high spectral resolution, the extraction of a number of valuable data is highly achieved(Xu, X. and Shi, Z., 2017). The growth of the earth observation technology caused the hyperspectral remote sensing imagery to be employed widely in environmental monitoring, exploration of minerals, and so on. The presence of mixed pixels as a result of poor spatial resolution and spatial complexity is the fundamental problem with HSI data (Gong et al., 2017). However, the recent advancements in hyperspectral sensors facilitate to obtain the images with high spectral resolution in the wide wavelength spectrum but mostly with spatial resolution challenges. Therefore, for the individual pixel, a near-continuous spectral signature is determined from the vast range of wavelengths and this significant property assures the observation and enables the identification of highly detailed and specific information of land-cover using the satellite images (Liu, S et al., 2016). Hyperspectral images providesthe information regarding the spatial position of the ground materials and assure the spectral signatures of individual pixel. The abundance in hyperspectral images assures the applicability in variousof applications (Wang, L et al., 2018).

Hyperspectral imaging gathers and processes the data in the electromagnetic spectrum and the hyperspectral image output holds the spectral information with high-resolution allowing the applications in variouss areas. However, the limited spatial resolution, along with the microscopic mixing of the material and multiple scattering causes the appearance of the mixed pixels in the obtained hyperspectral data. Thus, Spectral Unmixing (SU) becomes the significant technique for exploitation of the hyperspectral image, which led to the identification of the constituent spectra from the endmembers and caused the determination of their fractional abundances in the mixed pixel (Wang R. et al., 2017). The sparse unmixing strategy, which dealt with the inabilities for unmixingutilising complicated data and non-convex models (Gong et al., 2017), is one of the SU approaches to estimate fractional abundances of endmembers. SU identifies the constituent spectra or endmembers, and estimates the fractional abundances (N. Keshava et al. 2002). For the spectral unmixing, the mixing aspect in the mixed pixels are determined using the linear and non-linear mixture models (Bioucas-Dias et al., 2012 and N. Dobigeon et al. 2014), and the researchers are attracted because of the simplicity and proper physical meaning (Wang et al. 2017). SU dealt with the mixing issue and it is one of the active areas of interest. The traditional methods are summarized to possess two major steps: extraction of the endmember and inversion of the abundance (Bioucas-Dias et al., 2012 and Zhang S. et al. 2018). SU undergoes the decomposition of the spectral mixtures at pixel scale and enables the estimation of the quantitative abundance of materials (Uezato et al. 2018).

Among the variety of the SU methods, the method incorporated with the spatial information is found to be a significant approach. The hyperspectral image consists of multiple spatial homogeneous areas in which the material abundances possess same statistical inferences (Uezato et al. 2018). The linear mixture model includes the geometric (F. Chen and Y. Zhang 2013) and statistical methods (F. Schmidt et al. 2010) and using these methods, the endmembers are extracted directly from a scene, but the problem is regarding the extraction of the endmembers without any physical meaning. Among the presence of numerous spectral libraries, a semi supervised approach for sparse unmixing(M.D. Iordache et al. 2011), expresses the mixed pixels as pure spectral signatures. For determining the optimal endmembers, sparse regression methods are used, which is advantageous over the unsupervised approaches (Zhang et al. 2018 and J.W. Boardman, et al., 1995). The statistical methods exploit Bayesian paradigm to assure a natural paradigm to represent the change in endmembers, which led to generation of the endmembers along with their fractional abundances. To account for non negativity and additivity restrictions, the Bayesian approach (N. Dobigeon et al., 2014) constructs the unmixing using prior distributions on model variables. Additionally, the unmixing algorithms, like independent component analysis (ICA) (J. Bayliss et al. 1997) and nonnegative matrix factorization (NMF) (V. P. Pauca et al. 2006), are used, which belong to statistical approaches (Wang R. et al. 2017).

The goal of this research is to propose a multi-objective computing program for the SU with the hyperspectral satellite image by proposing an optimization algorithm. Here, a novel optimization algorithm, named Lion-Rider Optimization (LRO), is used for estimating the fractional abundance of every endmember by considering a linear sparse unmixing model. The proposed LRO algorithm is designed by the integration of Rider Optimization Algorithm (ROA) (Binu, D et al., 2018) and Lion Algorithm (LA) (Rajakumar, B.R., 2014) by making use of multiple objectives to optimize the reconstruction, sparsity, and total variation regularizations instantly. Here, a new objective function is developed by considering four objectives, namely Reconstruction Error (RSE), Sparsity (SPA), Spatial Neighbor (SNI), and Spatial Neighbour Correlation (SNC).

2. MOTIVATION

The motivation of the proposed research is to find an optimal algorithm to extract and quantify the endmembers and their corresponding fractional abundances from the mixed pixels of the given hyperspectral image.

2.1 Review of Literature

This section presents the review of ten existing sparse based spectral unmixing methods and aredicussed below:
(Xu, X., and Shi, Z., 2017) devised an approach known as the multi-objective optimization based sparse unmixing algorithm (MOSU), which proved to be more effective in tackling the sparse unmixing problem. The method's main flaw was the lack of a population-based approach, which

ISSN: 1992-8645 www.jatit.org E-ISSN: 1817-3195

would have improved computation efficiency. (Gong, M et al., 2017) developed Multi-objective Cooperative Coevolutionary algorithm, which directly optimized the non-convex norm problem and stood as the better compromise automatically for two or more competing cost function. The method failed for taking into account the parallel processing strategy. (Luo, W. et al., 2016) modelled the Biswarm particle swarm optimization (BiPSO) bilinear unmixing technique, which handled limited optimization and challenges owing to high-dimension by enabling an effective solution and ensuring a relatively flexible and easy means of tackling the SU issue. The method required a number of the complex non-linear models and estimation parameters. (Jiang, X., et al. 2018) used the Two-phase Multi-objective Sparse Unmixing (Tp-MoSU) framework that enabled the insights into the hyperspectral unmixing for the individual unmixing phases without the selection of regularization parameter, but the lack of parallel processing failed to utilize the merits of the multi-objective optimization. (Wang, R., et al. 2017) developed Centralized Collaborative Sparse Unmixing (CCSU) algorithm that reduced the estimation error and could perform the effective unmixing of the hyperspectral data and is failed in automatic detection.(Wang D. et al., 2018) developed a Sparse Redundant Unmixing (SpaRedU) algorithm, which effectively solved the spectral variation issue as a result of the substitution and it could effectively perform the estimation of the abundance. The method lacked the regularization of the redundant spectra in exploring the information related with the spatial–contextual data. (Wang, L., et al. 2018) developed an algorithm, Compressed Sensing Reconstruction that accurately estimated the total endmember from the spectral measurements with a higher value of the reconstruction accuracy and in addition, with less computational complexity. The method failed due to the lack of the high performance architectures for computing, like graphics processing in case of image reconstruction at the real-time application. (Liu, S et al., 2016) used the Multi-temporal Spectral Unmixing (MSU) approach that solved the multiple-change detection issue and permitted the detailed analysis over the spectral composition corresponding to a pixel. This approach is not significant for the advanced models investigation that would promote the outcome of unmixing.The multi-fidelity evolutionary multitasking optimization (MFEMO) framework is proposed (Li J. etal., 2021) to resolve the challenges in endmember extraction from the influence of outliers and expensive computation respectively. However, MFEMO includes inevitable negative transfer between tasks during endmember extraction which deteriorate the accuracy of endmember estimation].To handle large-scale sparse unmixing challenges, (Wang Z. et al., 2021) developed an evolutionary multi-objective hyperspectral sparse unmixing algorithm with endmember priori technique (EMSU-EP). Controlling noise in large-scale sparse unmixing issues is difficult using this technology]. (Xu X., et al., 2021) created a multiobjective-based simultaneous sparse unmixing framework (PMoSU), which considers reconstruction error, sparsity error, and the pruning projection function as three concurrent objectives for spectral unmixing in high-noise environments. In the case of discrete range sparse unmixing, weakly Pareto optimum solutions may emerge.

3. MATERIALS AND METHODS

In this section, the hyperspectral image representation is described and the methodology of the proposed Lion-Rider Optimization algorithm is explained.

The quantification of the endmembers from the hyperspectral image is achieved by the proposed spectral unmixing algorithm, which deliberates that hyperspectral image is a linear combination of spectra carrying vast proportion of endmembers in a pixel and in turn, the endmembers are weighed using the abundance factor. In general, spectral imaging record the scenes that consists of the spectral signatures arranged in a spectra, composed in a single pixel. Initially, the endmembers are estimated from a scene and then, the spectral signatures are identified, followed with the estimation of the fractional abundances in the individual endmember corresponding to the individual pixel. Even though all the existing methods follow the above steps, the existing methods suffer from the propagation errors and inaccuracy while estimating the endmembers. Moreover, the computational cost and complexity associated with the existing spectral unmixing processes remains high. So, to resolve all the above mentioned challenges, the research on spectral unmixing is done based on an optimization algorithm. Initially, the endmember is estimated and the proportion of the signature is estimated using the optimization algorithm. Lion Rider Optimization, which is developed using Rider Optimizaton Algorithm and Lion Optimization Algorithm. The estimation of the fractional

ISSN: 1992-8645 www.jatit.org E-ISSN: 1817-3195

abundance is considered using the multi-objective function, which is based on Sparsity, Spatial Neighbor, Reconstruction Error and Spatial Neighbor Correlation in a such a way that the accuracy is achieved. Figure 1 shows the conceptual diagram of the proposed Lion Rider Optimization Algorithm.

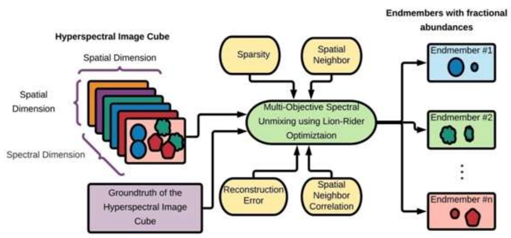

(Fig.1) Conceptual diagram of the proposed Lion-Rider optimization based multi-objective spectral unmixing algorithm

3.1 Hyperspectral Image Representation

Let us consider the hyperspectral image, which is represented in the matrix format as,

$$W = \{w_1, \ldots, w_m\} \in P^{u\times m} \quad (1)$$

where, $m$specifies the total spectra vectors and u refers to the spectral bands in the hyperspectral image. Based on the Linear Mixture Model (LMM), one can write the input image as,

$$W = Xp + N \text{such that } p \geq 0 1_q^T p = 1_m^T \quad (2)$$

where, $X = [x_1, \ldots, x_j, \ldots, x_q] \in P^{u\times q}$indicates the mixing matrix with $q$endmembers and $x_j$is the j^{th}signature of the endmember. The abundance matrix is denoted as, p, which in matrix format is given as,

$$p = [z_1, \ldots, z_j, \ldots, z_m] \in P^{q\times m} \quad (3)$$

The abundance matrix consists of the fractions of the endmembers and $z_j$refers to the j^{th}fraction of endmember in such a way that the pixel $j$varies between 1 and m.The sensing of the endmembers component-wise enables the better understanding of the abundance non-negativity constraint, which is denoted as $p \geq 0$. On the other hand, $1_q^T p = 1_m^T$signifies the sum-to-one constraint, which emerges from the physical interpretation of the abundance vector and $1_q = [1,1, \ldots, 1]^T$that refers to the column vector, which is of dimension$q$. The term $[\ \ ]^T$indicates the transpose of the vector elements. Similarly, Nin equation (1) refers to the noise that affects the measurement process. As a first step of spectral unmixing, the endmembers are determined or in other words, the endmembers $q$associated with the mixing matrix X and abundance matrix$p$. Let us assume that out of q endmembers $s$endmembers are estimated by the proposed algorithm. There are three conditionsas far as the total endmembers and estimated endmembers are concerned. The ideal situation arise when $q$and $s$are equal, whereas$s < q$symbolizes the underestimated state of the endmembers. The second condition enables the analysis for the easy identification of the more number of endmembers. On the other hand, $s > q$is the third condition where the overestimation of the endmembers occur, which would be the critical situation as that of condition 1 in such a way that there is no pure pixel existing in the captured image. In this paper, since $q$is not known in advance, the condition $s \geq$q, which is the overestimated state is considered. Thus, a common scenario prevails enabling the overestimation of the endmembers, which is easy to compute and this is not the actual case in case of the exact number of the endmembers. The estimation of q,$X$and p are performed based on the optimization algorithm depending on the multi-objective function.

3.2 Formulation of Spectral Unmixingmulti-Objective Function

The aim to estimate the endmembers and their abundance is achieved through proposing a new objective function, which is based on four constraints, such as RSE, SPA, SNC, and SNI respectively. The (Fig.1) depicts the conceptual diagram of the proposed lion-rider algorithm to optimize the spectral unmixing and(Jun Li, et al., 2016) reported that the objective function designed the following formula based on RSE, SPA, and SNI, which is given as,

$$\min_{G,Q} \left\{\frac{1}{2}\|W - GQ\|_J^e + \varepsilon\|Q\|_{2,1} + \frac{\eta}{2}\|G - M\|_J^e\right\} \text{such that } Q \in \Omega_{s-1} G \in E_{s-1} \quad (4)$$

where, $\|\ \ \|_J$and $\|\ \ \|_2$is the Frobenius and Euclidean norms, respectively. $G \equiv [n_1, \ldots, n_s] \in P^{u\times s}andQ \in P^{s\times m}$represent the optimization variables that is linked to the abundance and mixing matrices, respectively. The existing objective function in equation 4 specifies that the optimization aims at meeting the minimization objective function, which is based on three constraints, such as RSE, SPA, and SNI. The modified objective function is developed with the inclusion of the SNC term in equation 4 and is defined as,

$$\min_{G,Q}\left\{\frac{1}{2}\|W-GQ\|_J^e+\varepsilon\|Q\|_{2,1}+\frac{\eta}{2}\|G-M\|_J^e+\mu\left[\frac{1}{v*y*E}\sum_{i=1}^{v}\sum_{8}^{y}\left|\quad\right|\left|\quad\right|\right]\right\} \quad (5)$$

The optimization, LRO estimates the endmembers and their abundance using the multi-objective function formulated as in equation (5). The first term $\|W-GQ\|_J^e$represents the data fidelity that renders the solution with minimal reconstruction errors and the second term $\|Q\|_{2,1}$enables the row sparsity for the matrix Q through setting the complex rows at zero. The third term, $\frac{\eta}{2}\|G-M\|_J^e$drags the columns in Gtowards the solution M, which could be the solution of the algorithm that along with the matrix Qpulls the endmembers to the extreme that is defined by data$W$. The SPA is formulated as,

$$\|Q\|_{2,1}=\sum_{i=1}^{s}\|o\|_2 \quad (6)$$

The above equation specifies the mixed norm corresponding to matrix Q. The third term, SNI is given as,

$$\text{SNI}=\frac{\eta}{2}\|G-M\|_J^e \quad (7)$$

where, $M=[w_{i_1},\ldots,w_{i_s}]$refers to the set of $s$spectral vectors. The constants, $\varepsilon$and $\eta$are the regularization parameters. $\Omega_{s-1}$is a matrices of total dimension $(s\times m)$, where the columns belong to the probability simplex holding the dimension of $(s-1)$. Likewise, $E_{s-1}$are the matrix collections with size $(u\times s)$, and the columns are of size $(s-1)$, highlighting the data W. The objective function overcomes the drawback associated with the violation of the sum-to-one constraints that is generally available in real data. Additionally, the fourth term referred as the SNC, which is computed through subtracting the average of the neighboring pixels in the output image from each pixel of the original image.

The SNC is formulated as,

$$\text{SNC}=\mu\left[\frac{1}{v*y*E}\sum_{i=1}^{v}\sum_{8}^{y}\left|\quad\right|\left|\quad\right|\right] \quad (8)$$

where, $\mu$is the regularization parameter, $v$and $y$are the rows and columns in $(W-GQ)$. Thus, the estimation of endmembers is progressed using the LRO algorithm, which is explained in the section below.

3.3 Multi-objective Lion-Rider Optimization to Estimate the Fractional Abundance of the Endmembers

The fractional abundance of the individual endmember is estimated using the proposed LRO optimization, which is the modified ROA for which the LOA is integrated in the update rule of the bypass rider in such a way that the proposed LRO inherits the advantages of both the optimizations. Basically, ROA is based on non-realistic computing, engaged in solving the optimization problems using the assumptions.Furthermore, the algorithm is dependent on the riders' behaviour when they arrive at their destination. ROA render the ability of attaining the global solution through organizing the solutions in the form of the riders, bypass, over taker, follower, and attacker, and these riders update their positions based on the position of the leader. The leader is the leading rider in the race and is chosen based on the maximal success rate. Even though the performance of ROA is good, integrating LOA with ROA improves the ability of the algorithm towards dealing with the multi-objective functions. The LRO algorithm possesses better convergence with the maximal local optimal avoidance and global convergence in case of all the model functions. The steps of the proposed LRO are given below.

3.3.1 Initialization

The number of riders in the race and their positions are initialized in the first step,

$$L^\tau=L_{g,h}^\tau;(1\le g\le r);(1\le h\le d) \quad (9)$$

where, $r$refers to the total riders in the search space and $d$indicates the dimension or the total coordinates. $L_{g,h}^\tau$is the position of the g^{th}rider at $\tau$and the four categories of riders, bypass, overtaker, attacker, and follower are denoted as, B, O, A, and F. The riders in the above-mentioned groups are chosen equally from the total number of the riders, and it is noteworthy that each group of riders possess specific characteristics of riding. The bypass rider avoids the usual way to go to his destination, whereas the follower and attacker adjust their positions based on the leader, and the overtaker makes his own effort to get there. More importantly, excellent riding with the proper steering angle, gear, brake, and accelerator supports the rider in reaching the objective, despite the fact that each rider group has its own riding path. Thus, the riders adjust these parameters to update their positions and in addition, choosing the leader is the role of the success rate of the current instance until the off-time is approached. The term off-time refers to the time given for the race and the end of the off-time, the winner is announced and it is well known that the leading rider is different during the course of the race as each rider in the race varies the riding parameters in order to win. Let us represent the riding parameters of g^{th}rider, steering angle, coordinate angle, and position angle as, $\varphi^{\tau}_{g,h}$, $\psi^{\tau}_{g,h}$, and $C^{\tau}_{g,h}$. Moreover, the accelerator, gear, and brake of g^{th}rider is represented as, ω_g, κ_g, and b_g, respectively. The gear $\kappa_g$acquires a value between 0 and 4, while the values of ω_g, and b_g lie between 0 and 1.

3.3.2 Evaluating the success rate

The success rate of the solutions is determined using the multi-objective function formulated in equation (5), which should be as low as possible in order to find the best solution.

3.3.3 Update the location of the leading rider

The race's success rate is calculated, and the rider with the highest success rate is declared the leader, so that the attacker and follower riders can adjust their places based on the leader's position. The leader is a rider who is close to the finish line, and the interesting fact is that the leading rider does not always stay the same throughout the race, therefore the riders' success rate is assessed every now and then till the off-time is reached.

3.3.4 Rider position update phase

The riders, bypass, overtaker, attacker, and follower update their positions in this phase according to the position of the leading rider. The mathematical model of the riders' position is presented below:

3.3.5 Bypass riders' position

The bypassing nature of the bypass riders from the common way causes them to not follow the leader's course, which is modelled as,

$$L^{\tau+1}_{g,h}(B) = \beta\left[L^{\tau}_{a,g} * \alpha(g) + L^{\tau}_{\gamma,g} * \left(1-\alpha(g)\right)\right] \quad (10)$$

where, β, a, γ, and $\alpha$are the random numbers and the value of a, and γvary between 1 and r, whereas αvaries between 0 and 1. The dimension of α is given as, $(1\times d)$, where $d$specifies the dimension of the total coordinates. The bypass equation is modified using the LOA (Rajakumar, (2012), which is based on the Lion's social behavior, which live in pride and at the end of every generation; survival is the major cause, which insists on the strength of the generation. Each of the pride composes of 1-3 lions and their boundary of the peaceful interaction is defined and it is worth interesting that the Lions crossing the boundary are dragged for the fight including the nomads. Frequent territorial defence attack between the pride and the nomads occur and the one losing the (Fight is expelled out of the pride and killed. The social behavior of the lion is modelled as,

$$L^{\tau+1}_{g,h} = s^{\text{Fe}}_{g,h} + (0.1R_2 - 0.05)\left(s^{\text{Ma}}_{g,h} - R_1 s^{\text{Fe}}_{g,h}\right) \quad (11)$$

where, $g$refers to the vector elements, $s^{\text{Fe}}_{g,h}$symbolizes the g^{th}vector elements of female lion, $g$is the random integer in $[1, l]$. The length of the lion is denoted as, l and $L^{\tau+1}_{g,h}$is the updated equation of the female lion. Likewise, $s^{\text{Ma}}_{g,h}$specifies the g^{th}vector elements of the male lion, and R_1, $R_2$are the random numbers. Assume that the term, $L^{\tau}_{\gamma,g}$is equivalent to $L^{\tau+1}_{g,h}$ in equation 11. Thus, the following equation 12 is the derived by substituting the equation 11 in equation 10.

$$L^{\tau+1}_{g,h}(B) = \beta\left[L^{\tau}_{a,g} * \alpha(g) + s^{\text{Fe}}_{g,h} + (0.1R_2 - 0.05)\left(s^{\text{Ma}}_{g,h} - R_1 s^{\text{Fe}}_{g,h}\right) * \left(1-\alpha(g)\right)\right] \quad (12)$$

The suggested LRO algorithm's enhanced equation 12 highlights that the location of the bypass rider is updated based on the best position of the riders, random numbers, and the rider's position in the previous iteration.

3.3.6 Followers' position

The follower follows the leader to update the position and the position update is formulated as,

$$L^{\tau+1}_{g,h}(F) = L^{\text{Le}}_{\text{Le},h} + \left(\cos\left(\varphi^{\tau}_{g,h}\right) * L^{\text{Le}}_{\text{Le},h} * \varepsilon^{\tau}_{g}\right) \quad (13)$$

Let us denote the position of the leader as, $L^{\text{Le}}_{\text{Le},h}$, Le specifies the leading rider, $\varphi^{\tau}_{g,h}$is the steering angle corresponding to the g^{th}rider in h^{th}coordinate at time τ, $L^{\tau+1}_{g,h}(F)$specifies the position of the follower, and ε^{τ}_{g}denotes the distance covered by g^{th}rider at instant τ. The distance $\varepsilon^{\tau}_{g}$is calculated through multiplying the velocity and off-time. On the other hand, the velocity of the g^{th}rider is computed based on maximum speed, gear, accelerator, and brake corresponding to the vehicle of the g^{th}rider. The co-ordinate selector is chosen based on on-time probability, which depends on current instance τ, off-time, and total co-ordinates.

3.3.7 Overtakers' position

The placement of the overtaker depends on the coordinate selector, direction indicator, and success rate. The overtaker is modelled as,

$$L^{\tau+1}_{g,h}(O) = L^{\tau}_{g,h} + \left(D^{\tau}_{g} * L^{\text{Le}}_{\text{Le},h}\right) \quad (14)$$

where, $L^{\tau}_{g,h}$indicates the position of p^{th}rider in h^{th}coordinate and D^{τ}_{g}represents the direction indicator of g^{th}rider at τ. The direction indicator D^{τ}_{g} is calculated using the success rate as,

$$D^{\tau}_{g} = \left[\frac{2}{1-\log\left(\text{SuR}^{g}\right)}\right] - 1 \quad (15)$$

where, $\text{SuR}^{g}$is the success rate of g^{th}rider at τ, which is based on the multi-objective function. The coordinate selector is determined as the difference in position between the p^{th}rider and leading rider.

3.3.8 Attackers' position

The attacker is attempting to gain the leader's point, and the attacker's position update is comparable to that of the follower. The attacker formulates his or her position using the following formula:

$$L_{g,h}^{\tau+1}(A) = L_{\mathrm{Le},h}^{\mathrm{Le}} + \left[\cos\left(\varphi_{g,h}^{\tau}\right) * L_{\mathrm{Le},h}^{\mathrm{Le}} + D_g^{\tau}\right] \quad (16)$$

3.3.8 Re-compute the success rate

Riders update their positions based on the leader, and the success rate for all riders in the race is changed as a result. This represents the fact that the leading rider is not always the same and changes depending on the success rate.

3.3.9 Update the parameters of the rider

When all of the riders' success rates have been updated, the rider parameters must be modified in order to find the best option. Gear, accelerator, steering angle, brake, and off-time are the parameters used for the position update, with the addition of the parameter activity counter, which takes the value 0 or 1 depending on the success rate.

3.3.10 Termination

The optimization processes are performed until the race's end-of-race off-time. Based on the success rate, the best solution is found, and the winner is crowned, with the highest success rate among all the riders. Nothing but the fractional abundance of the solitary endmember is the best solution.

3.4 Proposed Algorithm

The pseudo code of the proposed Lion Rider Optimization algorithm is described below: The proposed LRO is amalgamation of ROA and LOA, i.e., in the ROA, updating the bypass riders' position is fused with the LOA algorithm so that the bypass rider always choose the best endmember from his decision. So, here the LOA is the subset of the ROA in achieving the best endmember extraction from the given hyperspectral image.

Algorithm 1. Pseudo code of Multi-Objective Lion-Rider Optimization

#	Lion-Rider Optimization
1	Input : Rider's position L^{τ}
2	Output : Leading rider $L_{\mathrm{Le},h}^{\mathrm{Le}}$
3	Start
4	Initialization
5	Rider population and riding parameters
6	Steering angle $\varphi_{g,h}^{\tau}$
7	Position angle $\psi_{g,h}^{\tau}$
8	Coordinate angle $C_{g,h}^{\tau}$
9	Gearκ_g
10	Acceleratorω_g
11	Brake b_g
12	Determine the success rate
13	While $\tau < \tau_{\mathrm{OFF}}$
14	For $(g = 1 to r)$
15	Update bypass riders' position (using lion social behavior) using eqn. (12)
16	Update the Overtakers' position depending on eqn. (14)
17	Update the position of Follower based on eqn. (13)
18	Follow eqn. (16) to update the position of attacker
19	Rank the riders based on the success rate
20	Determine the leading rider
21	Rider parameter update
22	Return $L_{\mathrm{Le},h}^{\mathrm{Le}}$
23	$\tau = \tau + 1$
24	End For
25	End While

4. RESULTS AND DISCUSSION

In this section, the findings of the spectral unmixing model for estimating the fractional abundance of endmember are demonstrated, with comparative results at the end of the section demonstrating the efficacy of the suggested method.

4.1 Experimental setup

The suggested SU technique is implemented in MATLAB, and the datasets utilised for spectral unmixing are Urban and Cuprite hyperspectral images from Datasets for unmixing (http://lesun.weebly.com/hyperspectral-data-set.html, 2020). The urban data is 307 × 307 pixels in a [2x2] metre square area, with 210 wavelengths spanning from 2500 to 400 nm with a spectral resolution of 10 nm.

For this urban data, there are about three ground truth versions, 4, 5, and 6 endmembers, which are introduced in the ground truth. The ground truth of the Urban dataset is chosen using a six-end-members version for this research. Asphalt, Metal, Roof, Grass, Dirt, and Tree are the six endmembers.

Cuprite data is separated into 224 channels, each with a wavelength spanning from 370 to 2480 nm. The area in question is 250 by 190 pixels and contains 14 different mineral types.Because there are minor changes between versions of related

Journal of Theoretical and Applied Information Technology
30th April 2022. Vol.100. No 8

ISSN: 1992-8645 www.jatit.org E-ISSN: 1817-3195

minerals, 12 endmembers have been recognised as the Cuprite dataset's ground truth data: Alunite, Buddingtonite, Andradite, Kaolinite1, Sphene, Dumortierite, Muscovite, Nontronite, Kaolinite2, Montmorillonite, Pyrope, and Chalcedony.

4.2 Experimental analysis

The experimental results depicts that the original Urban and Cuprite dataset image cubes, their original endmembers, and estimated endmembers using the proposed LRO-based spectral unmixing algorithm. (Fig.2)depicts the original hyperspectral image cubes. (Fig.2a) denotes Urban HSI and (Fig.2b) refers Cuprite HSI.

2a. Urban Hyperspectral Image Cube

2b. Cuprite Hyperspectral Image Cube
Figure.2. Hyperspectral Image Datasets

The original endmembers corresponding to the Urban HSI is depicted in (Fig.3) and are denoted as (Fig.3a) through (Fig. 3f).

3a. Asphalt

3b. Grass

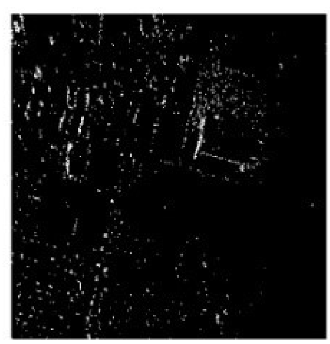

3c. Tree

ISSN: 1992-8645 www.jatit.org E-ISSN: 1817-3195

3d. Roof

3e. Metal

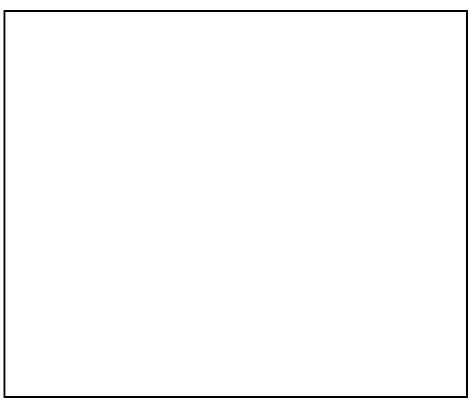

3f. dirt

Figure.3. Original endmembers corresponding to Urban image (Fig.3a). Asphalt, (Fig.3b).Grass, (Fig.3c).Tree, (Fig.3d).Roof, (Fig.3e).Metal and (Fig.3f). Dirt

Also, the original endmembers belongs to the Cuprite image are denoted as (Fig.4a) through (Fig. 4l).

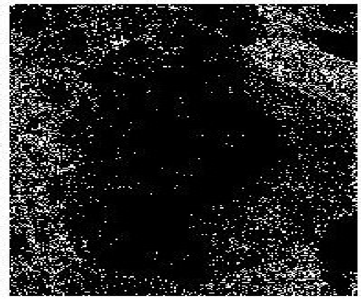

4a. Alunite

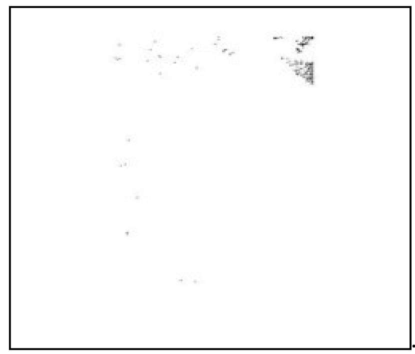

4b. Andradite

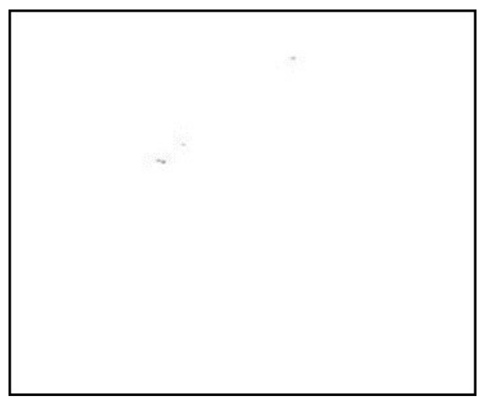

4c. Buddingtonite

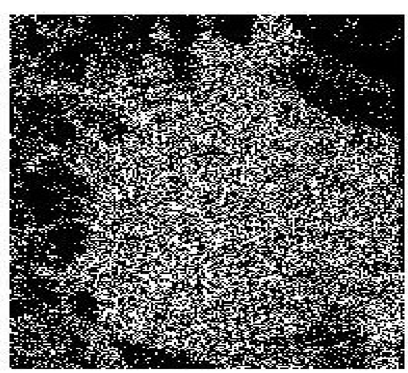

4d. Dumortierite

30th April 2022. Vol.100. No 8

ISSN: 1992-8645 www.jatit.org E-ISSN: 1817-3195

4e. Kaolinite1

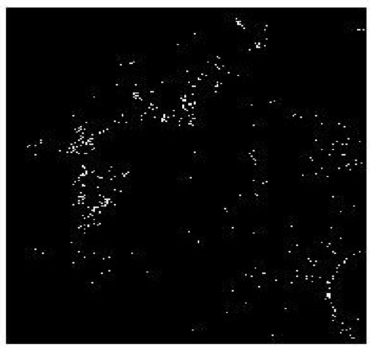

4f. Kaolinite2

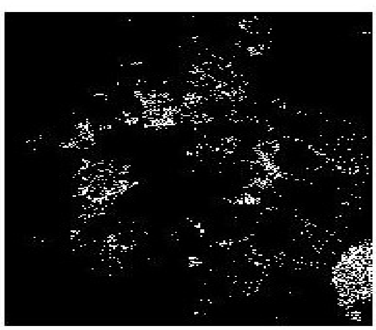

4g. Muscovite

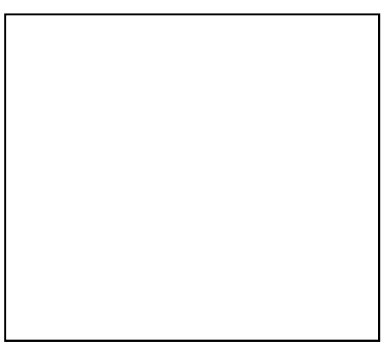

4h. Montmorillonite

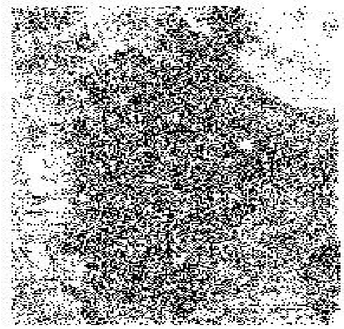

4i. Nontronite

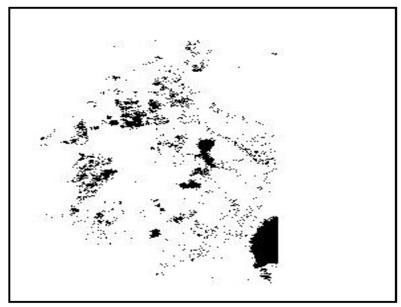

4j. Pyrope

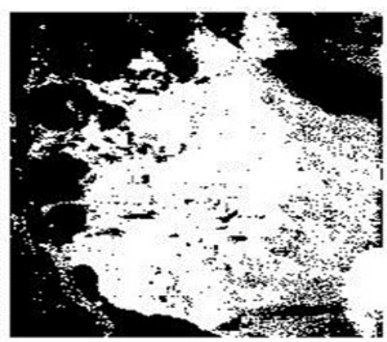

4k. Sphene

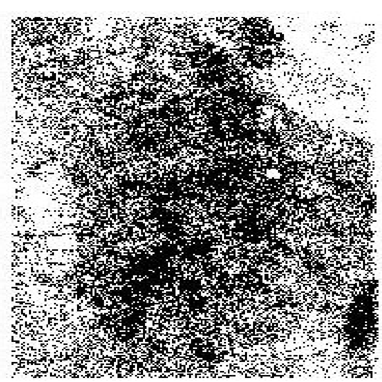

//////

4l. Chalcedony

Journal of Theoretical and Applied Information Technology
30th April 2022. Vol.100. No 8

ISSN: 1992-8645 www.jatit.org E-ISSN: 1817-3195

Figure .4. Original endmembers corresponding to Cuprite hyperspectral image (Fig.4a). Alunite, (Fig.4b).Andradite, (Fig.4c).Buddingtonite, (Fig.4d).Dumortierite, (Fig.4e).Kaolinite1, (Fig.4f). Kaolinite2, (Fig.4g). Muscovite, (Fig.4h).Montmorillonite, (Fig.4i).Nontronite, (Fig.4j).Pyrope, (Fig.4k).Spheneand (Fig. 4l).Chalcedony

The estimated endmembers of Urban HSI are represented in (Fig.5) from (Fig.5a) through (Fig.5f).

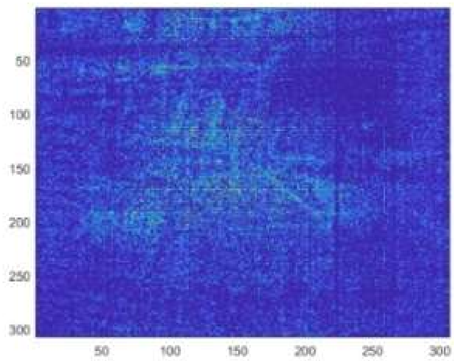

5a. Asphalt

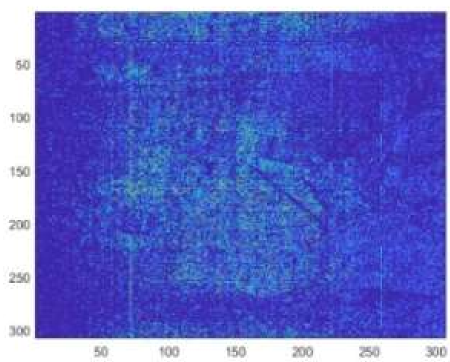

5b. Grass

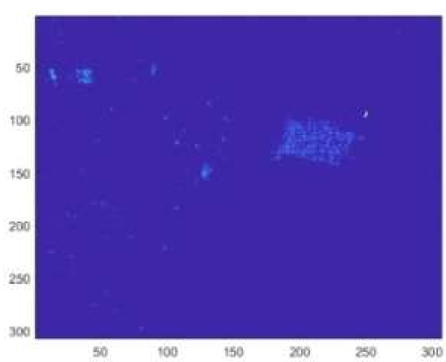

5c. Tree

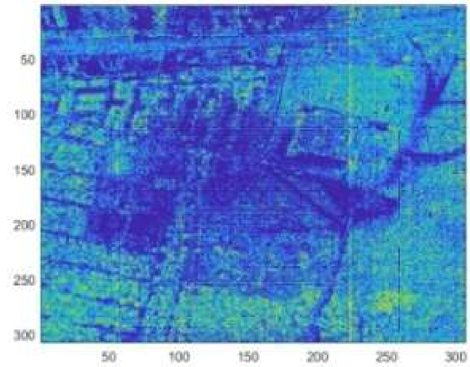

5d. Roof

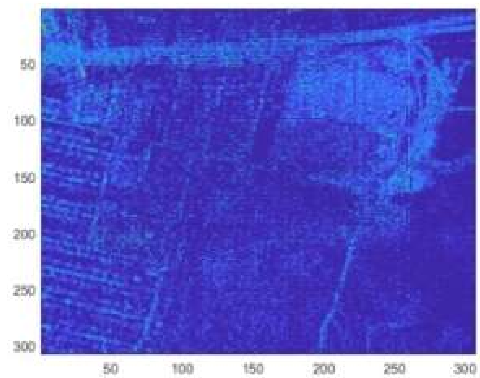

5e. Metal

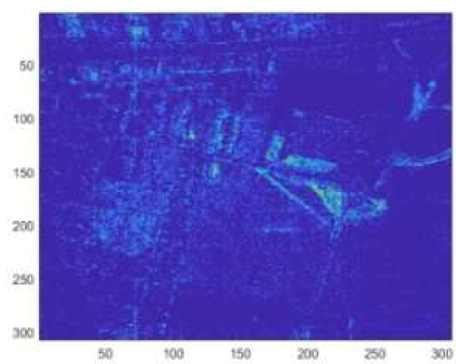

5f. Dirt

(Fig.5). Estimated endmembers corresponding to Urban image (Fig.5a). Asphalt, (Fig.5b). Grass, (Fig.5c). Tree, (Fig.5d).Roof, (Fig.5e).Metal and (Fig.5f). Dirt

Also, the estimated endmembers of Cuprite HSI are denoted in (Fig.6) from (Fig.6a) through (Fig.6l).

ISSN: 1992-8645 www.jatit.org E-ISSN: 1817-3195

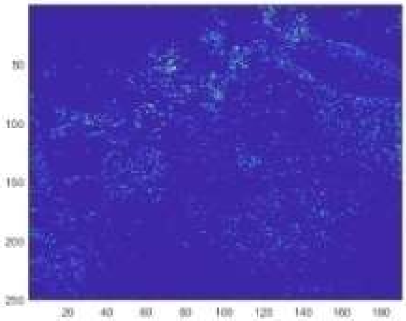

6a. Alunite

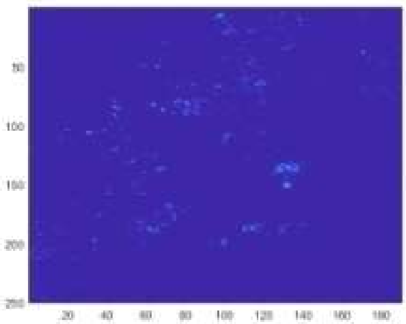

6b. Andradite

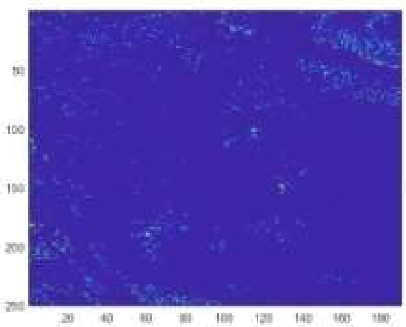

6c. Buddingtonite

6d. Dumortieriteib

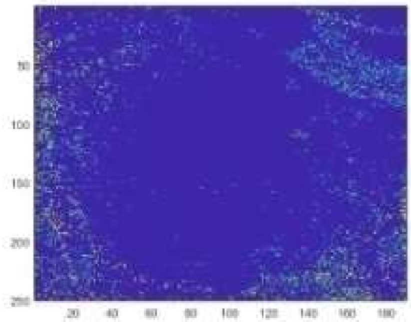

6e. Kaolinite1

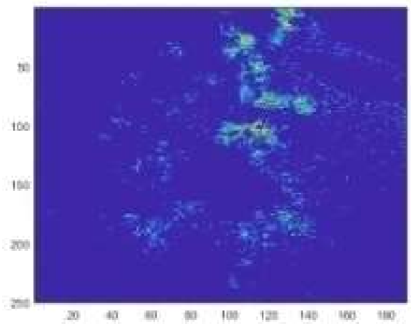

6f. Kaolinite2

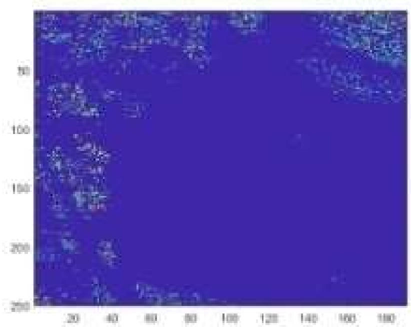

6g. Muscovite

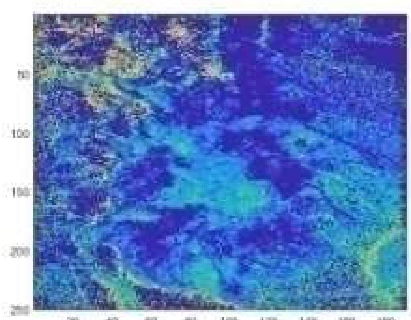

6h. Montmorillonite

ISSN: 1992-8645 www.jatit.org E-ISSN: 1817-3195

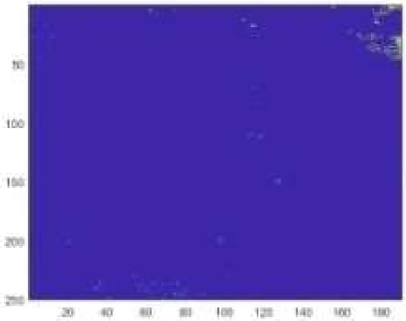

6i. Nontronite

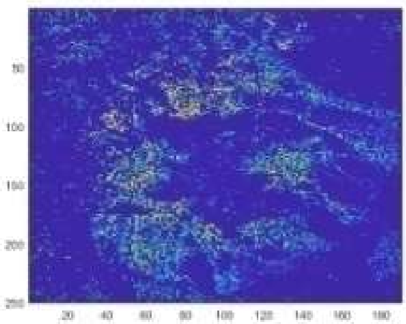

6j. Pyrope

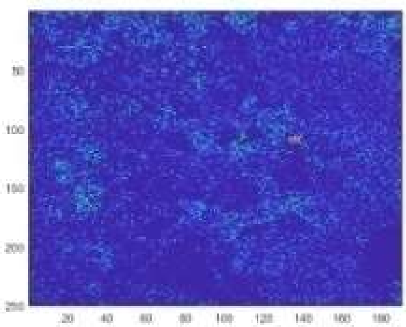

6k. Sphene

6l. Chalcedony

Figure .6. Estimated endmembers corresponding to Cuprite Hyperspectral Image (Fig.6a). Alunite, (Fig.6b).Andradite, (Fig.6c).Buddingtonite, (Fig.6d). Dumortierite, (Fig.6e). Kaolinite1, (Fig.6f). Kaolinite2, (Fig.6g). Muscovite, (Fig.6h).Montmorillonite, (Fig.6i).Nontronite, (Fig.6j).Pyrope, (Fig.6k).Spheneand (Fig.6l).Chalcedony

4.3 Performance Analysis using the Original endmembers

This section discusses the performance analysis of LRO algorithm using the endmembers in accordance with population size. (Fig.7) depicts the performance analysis using the endmembers of Urban image with respect to the bands. The analysis of the performance is done through changing the population size of LRO algorithm. (Fig.7a) shows the performance of endmember_1(Asphalt) with respect to the bands by varying the population size. When the band size is 50, the reflectance of LRO for population size 5, 10, 15, 20, and 25 are 0.0672%, -0.2461%, 0.1896%, -0.0076%, and 0.0058%. (Fig.7b) shows the performance of endmember_2 (Grass) with respect to the bands by changing the population size. When the band size is 50, the reflectance of LRO for population size 5, 10, 15, 20, and 25 are 0.1008%, -0.0148%, 0.0723%, 0.0275%, and 0.0204%. (Fig.7c) shows the performance of endmember_3 (Tree) with respect to the bands by moving population size. When the band size is 50, the reflectance of LRO for population size 5, 10, 15, 20, and 25 are 0.1318%, 0.0795 %, 0.0432 %, 0.0138 %, and 0.1677 %. (Fig.7d)shows the performance of endmember_4 (Roof) with respect to the bands by differ the population size. When the band size is 50, the reflectance of LRO for population size 5, 10, 15, 20, and 25 are -0.0276%, 0.0820%, 0.1590%, 0.0061%, and 0.1156%. (Fig.7e) shows the performance of endmember_5 (Metal) with respect to the bands by varying the population size. When the band size is 50, the reflectance of LRO for population size 5, 10, 15, 20, and 25 are 0.0578%, -0.0934%, -0.0921%, -0.0198%, and 0.0625%. (Fig.7f) shows the performance of endmember_6 (Dirt)with respect to the bands by the dynamic population size. When the band size is 50, the reflectance of LRO for population size 5, 10, 15, 20, and 25 are 0.0703%, -0.0434%, 0.2037%, 0.1222%, and 0.1942%.

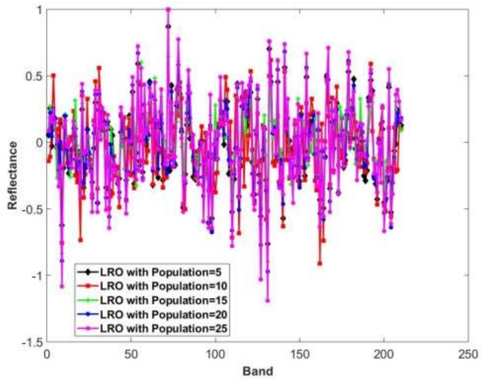

7a. Performance analysis of Asphalt

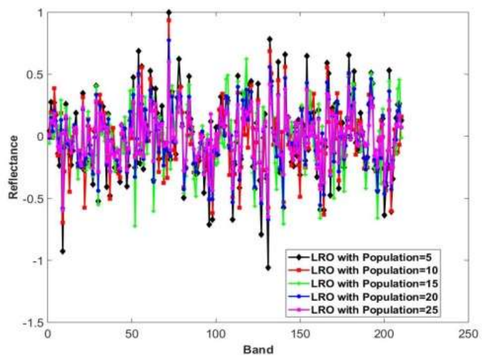

7b. Performance analysis of Grass

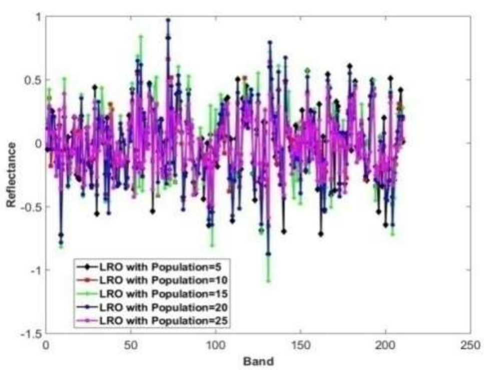

7c. Performance analysis of Tree

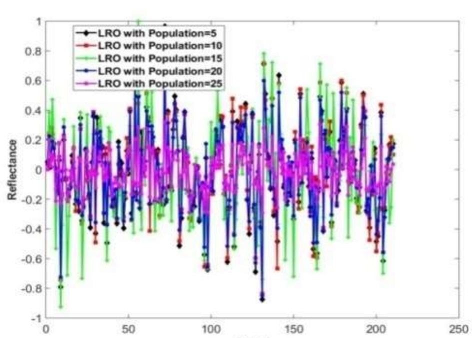

7d. Performance analysis of Roof

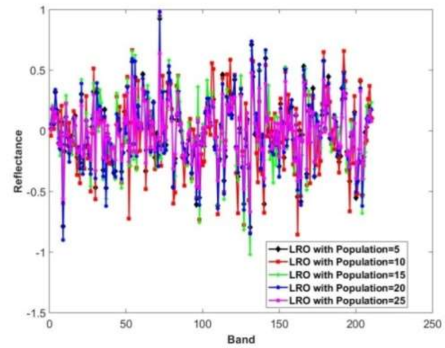

7e. Performance analysis of Metal

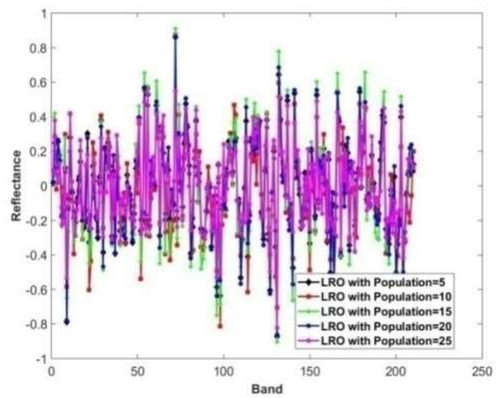

7f. Performance analysis of Dirt

(Fig.7). Performance analysis of the end members of Urban Image
(Fig.7a). Asphalt, (Fig.7b).Grass, (Fig.7c).Tree, (Fig.7d).Roof, (Fig.7e).Metal and (Fig.7f). Dirt

The second part of this section depicts the performance analysis using the endmembers of Cuprite image with respect to the bands. (Fig.8)shows the performance analysis using the endmembers with respect to the number of bands and the performance analysis is performed by varying the population size of LRO algorithm. (Fig.8a) shows the performance analysis of end member_1 (Alunite) with respect to the bands by varying the population size. When the band size is 50, the reflectance of LRO for population size 5, 10, 15, 20, and 25 are 0.0943%, 0.1539%, 0.1086%, -0.0932%, and 0.0195%. (Fig.8b) shows the performance analysis of end member_2 (Andradite) with respect to the bands by varying the population size. When the band size is 50, the reflectance of LRO for population size 5, 10, 15, 20, and 25 are 0.1156%, 0.2129%, 0.1742%, 0.2016%, and 0.2157%. (Fig.8c) shows the performance analysis of end member_3

(Buddingtonite) with respect to the bands by varying the population size. When the band size is 50, the reflectance of LRO for population size 5, 10, 15, 20, and 25 are 0.0671%, -0.0200%, 0.1446%, 0.1995%, and 0.0522%. (Fig.8d) shows the performance analysis of endmember_4 (Dumortierite) with respect to the bands by varying the population size. When the band size is 50, the reflectance of LRO for population size 5, 10, 15, 20, and 25 are 0.1484%, 0.3048%, 0.1172%, 0.3940%, and -0.1047%. (Fig.8e) shows the performance analysis of endmember_5 (Kaolinite1) with respect to the bands by varying the population size. When the band size is 50, the reflectance of LRO for population size 5, 10, 15, 20, and 25 are 0.2235%, 0.0892%, -0.1511%, 0.1967%, and 0.1094%. (Fig.8f) shows the performance analysis of end member_6 (Kaolinite2) with respect to the bands by varying the population size. When the band size is 50, the reflectance of LRO for population size 5, 10, 15, 20, and 25 are 0.2288%, 0.2146%, 0.0316%, 0.1019%, and -0.0488%. (Fig.8g) shows the performance analysis of endmember_7 (Muscovite) with respect to the bands by varying the population size. When the band size is 50, the reflectance of LRO for population size 5, 10, 15, 20, and 25 are 0.0635%, -0.0416%, 0.1899%, 0.0477%, and 0.0635%. (Fig.8h) shows the performance analysis of endmember_8 (Montmorillonite) with respect to the bands by varying the population size. When the band size is 50, the reflectance of LRO for population size 5, 10, 15, 20, and 25 are 0.1242%, 0.0657%, -0.0267%, 0.2579%, and 0.0251%.(Fig.8i) shows the performance analysis of end member_9 (Nontronite) with respect to the bands by varying the population size. When the band size is 50, the reflectance of LRO for population size 5, 10, 15, 20, and 25 are 0.0736%, 0.0306%, 0.0618%, -0.1568%, and -0.0518%. (Fig.8j) shows the performance analysis of endmember_10 (Pyrope) with respect to the bands by varying the population size. When the band size is 50, the reflectance of LRO for population size 5, 10, 15, 20, and 25 are 0.0662%, 0.0136%, -0.2766%, -0.0501%, and 0.3449%. (Fig.8k) shows the performance analysis of endmember_11 (Sphene) with respect to the bands by varying the population size. When the band size is 50, the reflectance of LRO for population size 5, 10, 15, 20, and 25 are 0.1550%, 0.2085%, 0.0775%, 0.0797%, and -0.0532%. (Fig.8l) shows the performance analysis of endmember_12 (Chalcedony) with respect to the bands by varying the population size. When the band size is 50, the reflectance of LRO for population size 5, 10, 15, 20, and 25 are 0.2741%, 0.1906%, 0.3113%, 0.2889%, and 0.0675%.

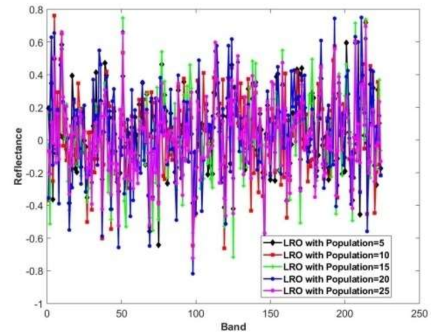

8a. Performance analysis of Alunite

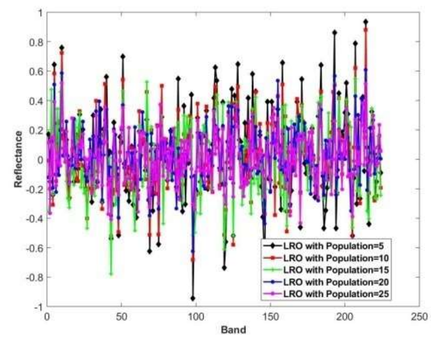

8b. Performance analysis of Andradite

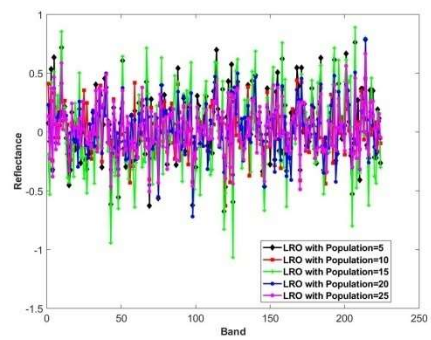

8c. Performance analysis of Buddingtonite

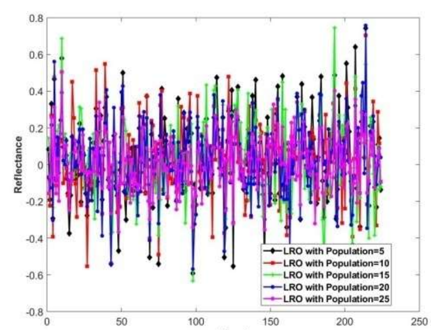

8d. Performance analysis of Dumortieriteb

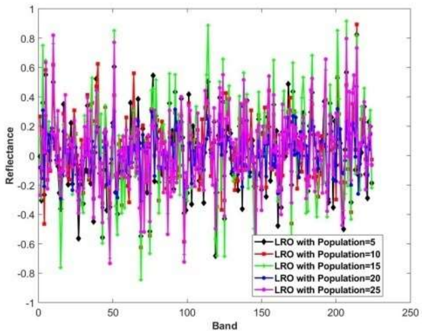

8e. Performance analysis of Kaolinite1

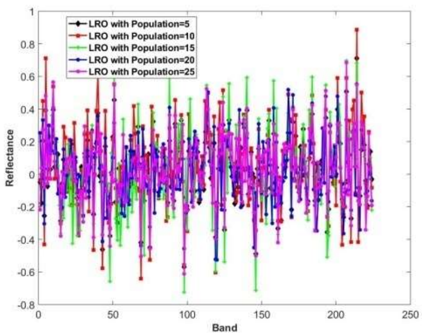

8f. Performance analysis of Kaolinite2

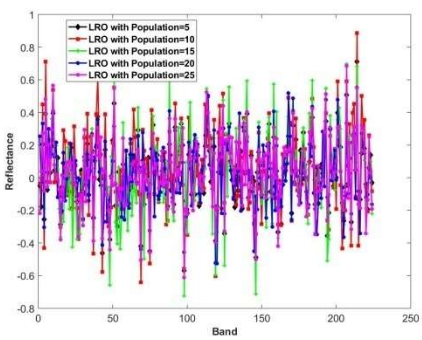

8g. Performance analysis of Muscovite

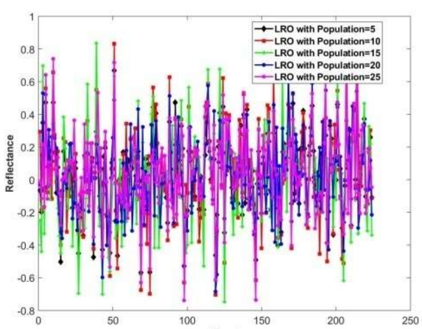

8h. Performance analysis of Montmorillonite

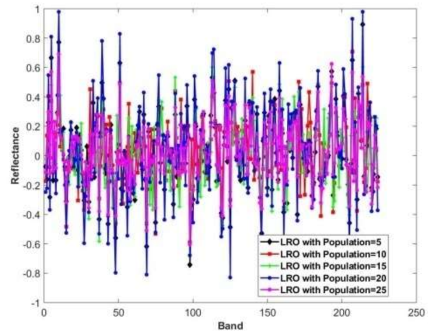

8i. Performance analysis of Nontronite

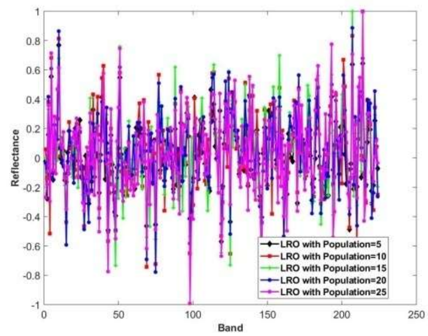

8j. Performance analysis of Pyrope

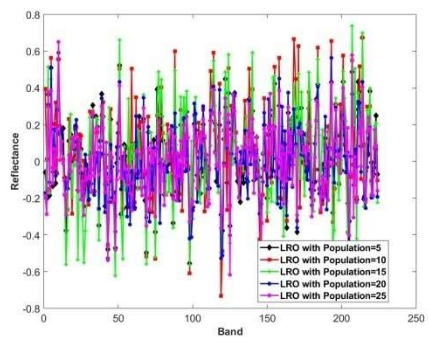

8k. Performance analysis of Sphene

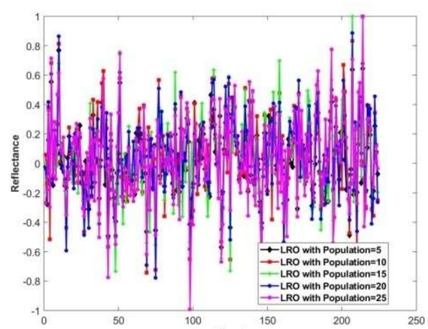

8j. Performance analysis of Pyrope

Journal of Theoretical and Applied Information Technology
30th April 2022. Vol.100. No 8

ISSN: 1992-8645 www.jatit.org E-ISSN: 1817-3195

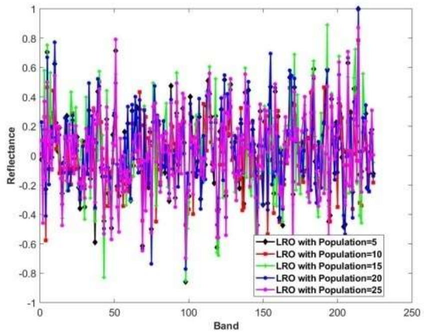

8l. Performance analysis of Chalcedony

Figure .8. Performance analysis of the end members of Cuprite Image (Fig.8a). Alunite, (Fig.8b).Andradite, (Fig.8c).Buddingtonite, (Fig.8d). Dumortierite, (Fig.8e). Kaolinite1, (Fig.8f). Kaolinite2, (Fig.8g). Muscovite, (Fig.8h). Montmorillonite, (Fig.8i). Nontronite, (Fig.8j).Pyrope, (Fig.8k).Spheneand (Fig.8l). Chalcedony

4.4 Performance Metrics

For comparison with existing research, the performance of the proposed SU approach is tested using two metrics: root mean square error (RMSE) and reconstruction error (RE). The RMSE of the methods is calculated as follows:

$$RMSE_j = \sqrt{\frac{1}{u}\sum_{j=1}^{u}\left(x_{ij} - \hat{x}_{ij}\right)^2} \tag{17}$$

where, u refers to the total pixel, x_{ij} signifies the real abundance fraction for i^{th} endmember in j^{th} pixel, and $\hat{x}_{ij}$ refers to the corresponding estimated value. Thus,

$$RMSE = \sum_{j=1}^{q} RMSE_j \tag{18}$$

where, $q$symbolizes the extracted endmembers and $RMSE_j$ corresponds to the RMSE of the individual pixels. Any effective method reports with the minimal value of RMSE to symbolize the effective performance. The RE of the methods is computed as,

$$RE = \left\| z - \hat{z} \right\|_{ff}^{2} \tag{19}$$

where, z refers to the true abundance matrix and $\hat{z}$ indicates the estimated abundance matrix. The accurate estimation is indicated by the smaller value of RE. The reflectance of a pixel is given as,

$$W_j = \sum_{j=1}^{u} X_{ij}\, P_j + N_i \tag{20}$$

where, W_j specifies the measured reflectance of an individual pixel at spectral band j, X_{ij} refers to the reflectance of j^{th} endmember at the spectral band j, N_i indicates the errors for the band j, and P_j symbolizes the fractional abundance of j^{th} endmember.

4.5 Performance Analysis based on the Performance Metrics

The performance of the LRO approach with varying population size is examined in this section using performance indicators such as RE and RMSE. The performance study based on performance measures of both Urban and Cuprite images is shown in (Fig.9). The performance of Urban image based on RE is depicted here. The RE analysis based on SNR is done with respect to the population size of LRO. When the SNR is 25 dB, the RE of LRO is 22.8794, 24.9163, 21.1923, 16.5803, and 23.3827 when the population size is 5, 10, 15, 20, and 25, respectively. (Fig.9b) shows the performance of Urban image based on RMSE. The RMSE analysis based on SNR is done with respect to the population size of LRO. When the SNR is 25 dB, the RMSE of LRO is 0.0304, 0.0331, 0.0282, 0.0220, and 0.0311 when the population size is 5, 10, 15, 20, and 25, respectively.(Fig.9c) shows the performance of Cuprite image based on RE. The RE analysis based on SNR is done in accordance with the population size of LRO. When the SNR is 25 dB, the RE of LRO is 24.8878, 30.8841, 37.0341, 28.2251, and 29.7265when the population size is 5, 10, 15, 20, and 25, respectively. (Fig.9d) shows the performance of Cuprite image based on RMSE. The RMSE analysis based on SNR is done with respect to the population size of LRO. When the SNR is 25 dB, the RMSE of LRO is 0.0330, 0.0409, 0.0491, 0.0374, and 0.0394 when the population size is 5, 10, 15, 20, and 25, respectively.

ISSN: 1992-8645 www.jatit.org E-ISSN: 1817-3195

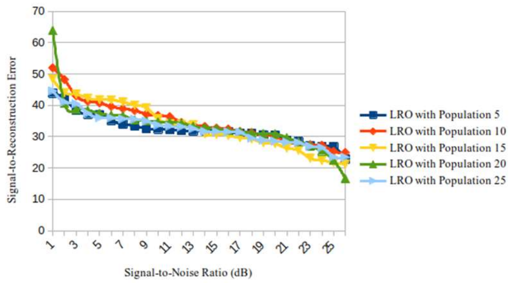

9a. Reconstruction error of Urban image

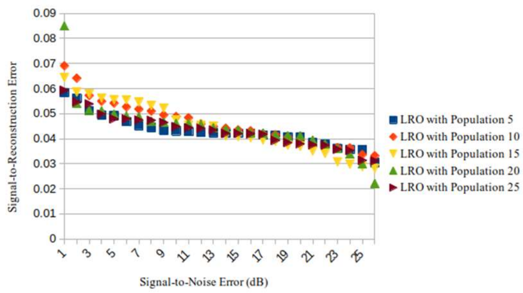

9b. Root mean square error of Urban image

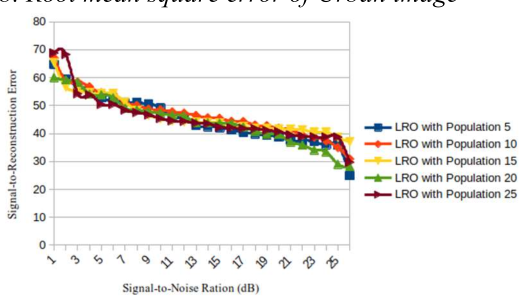

9c. Reconstruction error of Cuprite image

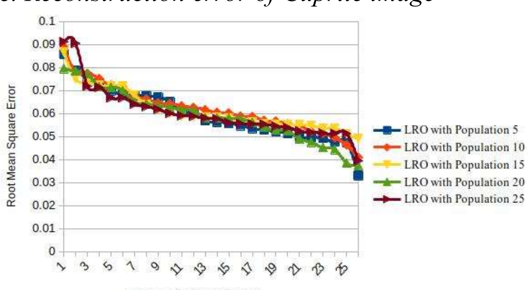

9d. Root mean square error of Cuprite image

Figure .9. Performance analysis based on the performance metrics
(Fig.9a). Reconstruction error of Urban image, (Fig.9b). Root mean square error of Urban image, (Fig.9c). Reconstruction error of Cuprite image, (Fig.9d). Root mean square error of Cuprite image

4.6 Comparative Methods

The comparative methods used for the comparison of the performance of LRO includes: bi-objective optimization model (Bi-MOSU) and tri-objective optimization model (Tri-MOSU) (Gong M. et al., (2017), Robust collaborative Non-negative matrix Factorization (R-CoNMF) (Jun L. et al., 2016), Pareto multi-objective based sparse unmixing (Pareto- MOSU) (Xu X. et al., 2017), and Rider Optimization Algorithm (ROA) (Binu D. et al., 2018).

4.7 Comparative Analysis using the endmembers

The performance of LRO employing Urban and Cuprite over rival algorithms is reviewed in this section. The comparative analysis using the end members of the Urban picture is shown in Figure 10. From (Fig. 10a) to (Fig. 10f), the competing methods Bi-MOSU + Tri-MOSU, R-CoNMF, Pareto-MOSU, ROA, and suggested LRO have obtained reflectances of 0.0880 percent, -0.3422 percent, -0.1965 percent, -0.0625 percent, and -0.3891 percent, respectively, at the band of 45. When these values are compared to the existing approaches, it is obvious that the proposed method has a higher reflectivity.

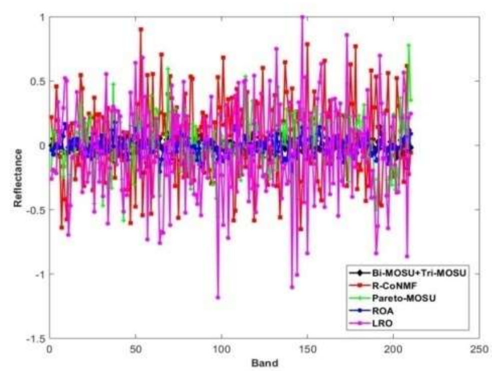

10a. Comparative analysis of Asphalt

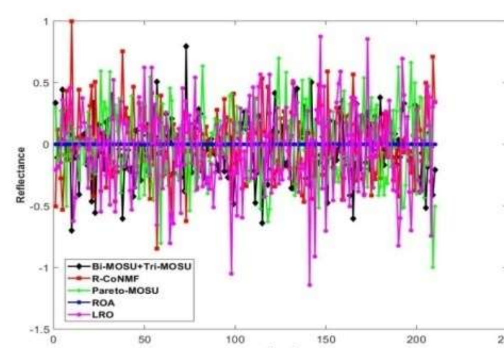

10b. Comparative analysis of Grass

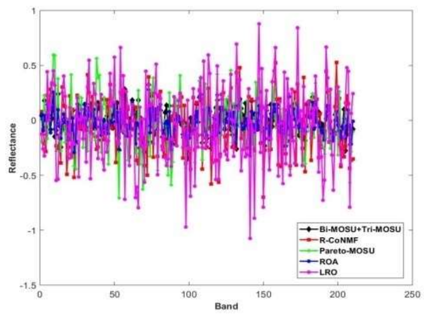

10c. Comparative analysis of Tree

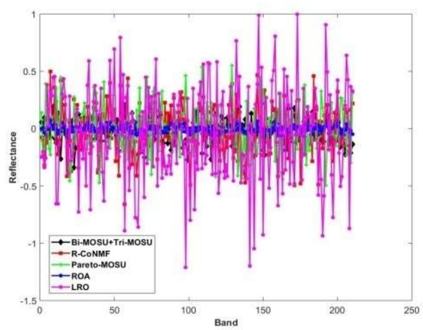

10d. Comparative analysis of Roof

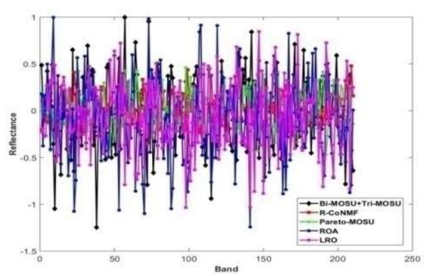

10e. Comparative analysis of Metal

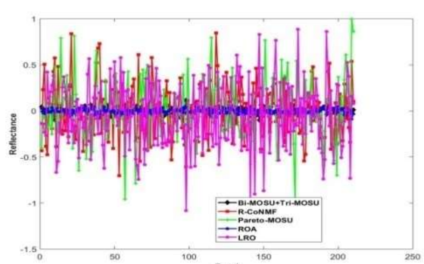

10f. Comparative analysis of Dirt

(Fig.10). Comparative analysis of LRO with competing methods for Urban image endmembers (Fig.10a). Asphalt, (Fig.10b). Grass, (Fig. 10c). Tree, (Fig.10d).Roof, (Fig.10e).Metal and (Fig.10f). Dirt

The comparative analysis performed using the endmembers from Cuprite image. Upon analysis, as depicted in (Fig.11 (Fig.11a) through (Fig.11l), the reflectance of the proposed LRO algorithm is -0.0417%, 0.0300%, 0.0092%, 0.0453%, -0.0071%, -0.0295%, 0.0211%, 0.0013%, 0.1185%, 0.1427%, -0.0225%, and -0.067%, respectively when the band is 224.

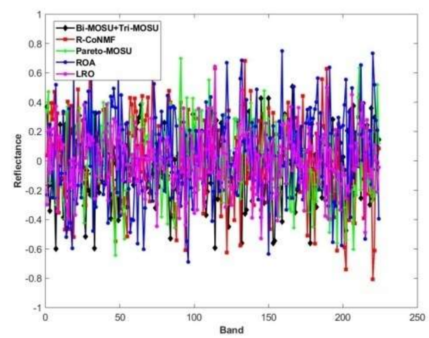

11a. Comparative analysis of Alunite

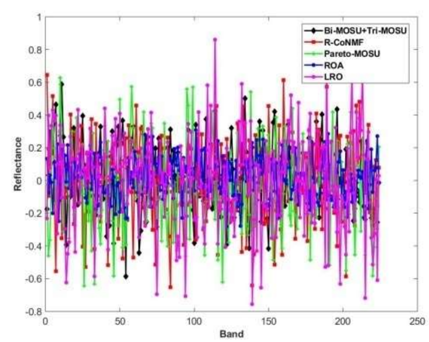

11b. Comparative analysis of Andradite

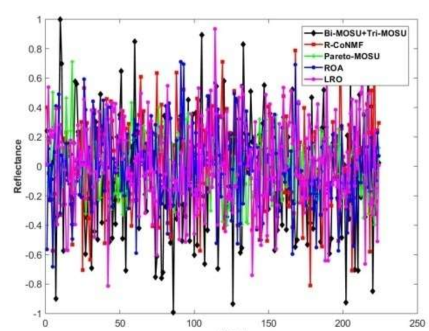

11c. Comparative analysis of Buddingtonite

ISSN: 1992-8645 www.jatit.org E-ISSN: 1817-3195

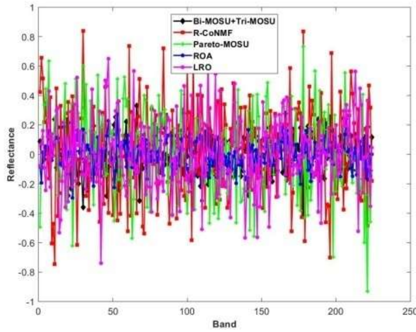

11d. Comparative analysis of Dumortieritei

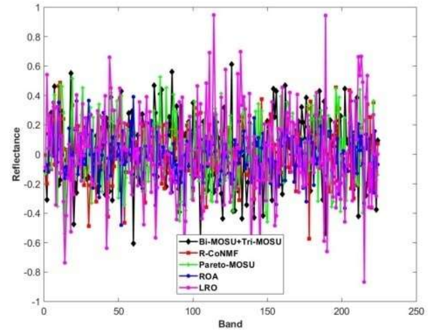

11h. Comparative analysis Montmorillonite

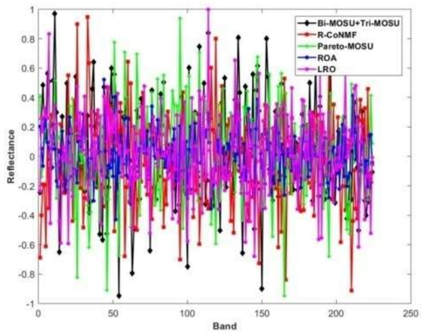

11e. Comparative analysis of Kaolinite1

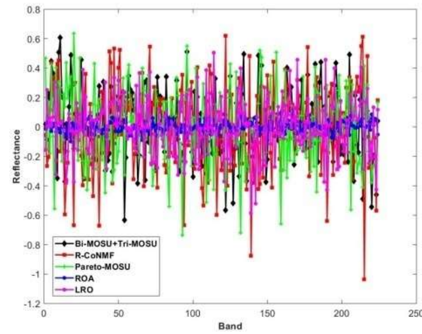

11i. Comparative analysis Nontronite

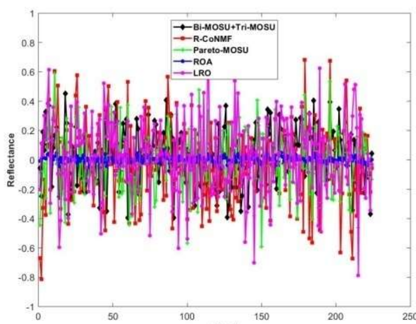

11f. Comparative analysis of Kaolinite2

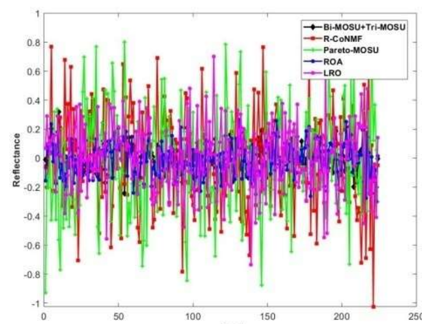

11j. Comparative analysis of Pyrope

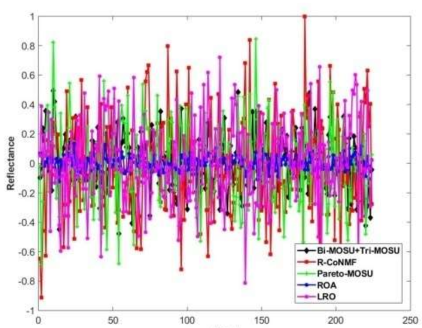

11g. Comparative analysis of Muscovite

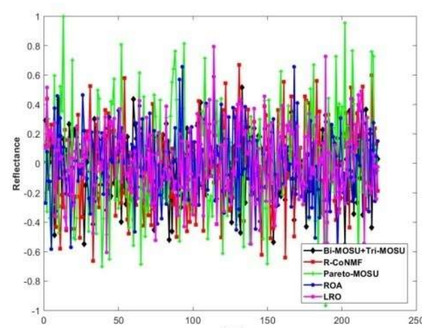

11k. Comparative analysis of Sphene

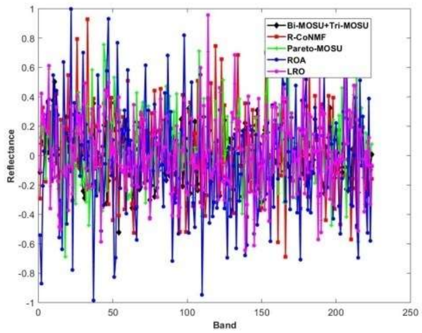

11l. Comparative analysis of Chalcedony

Figure 11 - . Comparative analysis using the endmembers of Urban image
(Fig.11a). Alunite, (Fig.11b).Andradite, (Fig.11c).Buddingtonite, (Fig.11d). Dumortierite, (Fig.11e). Kaolinite1, (Fig.11f). Kaolinite2, (Fig.11g). Muscovite, (Fig.11h). Montmorillonite, (Fig.11i). Nontronite, (Fig.11j).Pyrope, (Fig.11k).Sphene and (Fig.11l). Chalcedony

4.8 Comparative Analysis Based on the Performance Metrics

This section demonstrates a comparison study based on performance measures. Based on the performance criteria, (Fig.12) displays a comparison of the Urban and Cuprite images. The comparative analysis employing an urban image based on RE is shown in (Fig. 12a).The RE of the methods, Bi-MOSU + Tri-MOSU, R-CoNMF, Pareto-MOSU, ROA, and proposed LRO is 24.9163, 23.3827, 21.1923, 22.8794 and 16.5803 when the SNR is 25dB. (Fig.12b) shows the comparative analysis using Urban image based on RMSE. The RMSE of the methods, Bi-MOSU + Tri-MOSU, R-CoNMF, Pareto-MOSU, ROA, and proposed LRO is 0.03311, 0.0282, 0.0311, 0.0304 and 0.022 when the SNR is 25dB. (Fig.12c) shows the comparative analysis using original Cuprite image based on RE. The RE of the methods, Bi-MOSU + Tri-MOSU, R-CoNMF, Pareto-MOSU, ROA, and proposed LRO is 30.8841, 29.7265, 37.0241, 24.8878 and 28.2251 when the SNR is 25dB. (Fig.12d) shows the comparative analysis using Cuprite image based on RMSE. The RMSE of the methods, Bi-MOSU + Tri-MOSU, R-CoNMF, Pareto-MOSU, ROA, and proposed LRO is 0.0409, 0.0491, 0.0394, 0.033 and 0.0374respectively, when the SNR is 25dB.

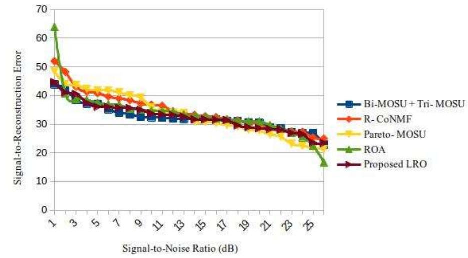

12a. Reconstruction error of Urban image

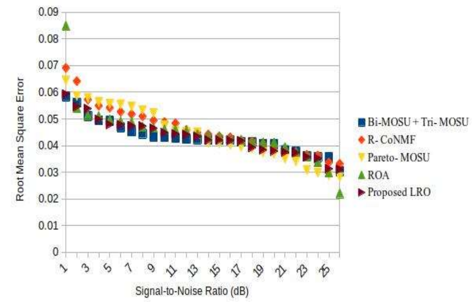

12. Root mean square error of Urban image

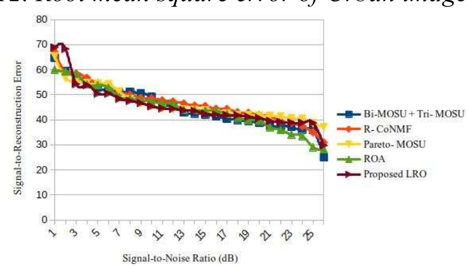

12c. Reconstruction error of Cuprite image

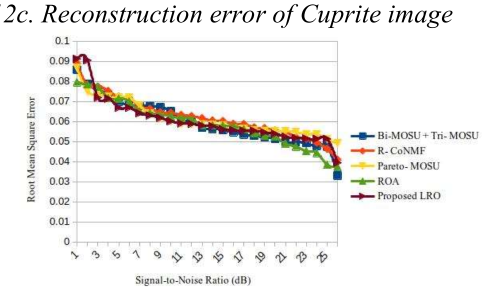

12d. Root mean square error of Cuprite image

Figure 12. Comparative analysis using performance metrics,
(Fig.12a). Reconstruction error of Urban image, (Fig.12b). Root mean square error of Urban image, (Fig.12c). Reconstruction error of Cuprite image and (Fig.12d). Root mean square error of Cuprite image

The Table 1 provides the comparison of performance metrics related to the effectiveness of the proposed LRO algorithm in spectral unmixing. It is witnessed from Table 1 that the proposed LRO spectral unmixing outperformed the competing methods with a minimal RMSE and minimal RE of 0.0297 and 22.4027, respectively.

Table 1. Comparative discussion of the performance of Lion-Rider optimization with competitive algorithms

Metrics	Bi-MOSU + Tri-MOSU	R- CoNMF	Pareto-MOSU	ROA	Proposed LRO
RMSE	0.037005	0.03865	0.03525	0.0317	0.0297
RE	27.9002	26.5546	29.1082	23.8836	22.4027

5 CONCLUSION

This research demonstrates how to use spectral unmixing to estimate endmembers and their fractional abundances from mixed pixels. The spectral unmixing is handled based on the optimization algorithm, called Lion Rider Optimization (LRO) which uses the multi-objective function modelled using the optimization factors, namely Reconstruction Error (RSE), Sparsity (SPA), Spatial Neighbor (SNI), and Spatial Neighbour Correlation (SNC). The linear sparse unmixing model based on the proposed LRO estimates the fractional abundances from the endmembers. The proposed method is theenhancement of the Rider optimization algorithm which uses the Lion optimization algorithm as an integral component. The analysis of the methods is performed using the Urban and Cuprite datasets and evaluated using the performance metrics of RMSE and RE.From this research study, it is witnessed that the proposed LRO algorithm outperformed the competing techniques with aa minimal RE and minimal RMSE values of 22.4027 and 0.0297, respectively. It is learned that the estimation of the fractional abundance from the estimated endmembers is done effectively and with notable accuracy. The future work on this research may incorporate various bio-inspired optimization approaches for further exploration of information from the hyperspectral images with optimal computing cost and better accuracy.

DECLARATION OF COMPETING INTEREST STATEMENT

None of this work has previously been published, has been accepted for publication in another journal, or is currently being reviewed in another journal. There are no conflicts of interest among the authors.

REFERENCES:

[1]. Binu, D., &Kariyappa, B. S. (2018). RideNN: A New Rider Optimization Algorithm-Based Neural Network for Fault Diagnosis in Analog Circuits. IEEE Transactions on Instrumentation and Measurement, 68(1), 2–26. https://doi.org/10.1109/TIM.2018.2836058

[2]. Bioucas-Dias, J. M., Plaza, A., Dobigeon, N., Parente, M., Du, Q., Gader, P., &Chanussot, J. (2012). Hyperspectral unmixing overview: Geometrical, statistical, and sparse regression- based approaches. In IEEE Journal of Selected Topics in Applied Earth Observations and Remote Sensing. https://doi.org/10.1109/JSTARS.2012.2194696

[3]. Boardman, J. W., Kruse, F. a., & Green, R. O. (1995). Mapping target signatures via partial unmixing of AVIRIS data. Summaries of JPL Airborne Earth Science Workshop, 3–6. http://citeseerx.ist.psu.edu/viewdoc/download?doi=10.1.1.26.4610&rep=rep1&type=pdf

[4]. Chen, F., & Zhang, Y. (2013). Sparse hyperspectral unmixing based on constrained ℓp - ℓ2 optimization. IEEE Geoscience and Remote Sensing Letters, 10(5), 1142–1146. https://doi.org/10.1109/LGRS.2012.2232901

[5]. Datasets for unmixing, http://lesun.weebly.com/hyperspectral-data-set.html accessed on 19th August 2020.

[6]. Dobigeon, N., Moussaoui, S., Coulon, M., Tourneret, J. Y., & Hero, A. O. (2009). Joint Bayesian endmember extraction and linear unmixing for hyperspectral imagery. IEEE Transactions on Signal Processing, 57(11), 4355–4368. https://doi.org/10.1109/TSP.2009.2025797

[7]. Dobigeon, N., Tourneret, J., Richard, C., & Images, H. (2014). Nonlinear Unmixing of Hyperspectral Images [. January, 82–94.

[8]. Gong, M., Li, H., Luo, E., Liu, J., & Liu, J. (2017). A Multiobjective Cooperative Coevolutionary Algorithm for Hyperspectral Sparse Unmixing. IEEE Transactions on Evolutionary Computation, 21(2), 234–248. https://doi.org/10.1109/TEVC.2016.2598858

[9]. Jessica Beyliss, J.AnthonyGualtieri, & Robert F. Cromp. (2015). Analyzing Hyperspectral

data with Independent Component Analysis. Spie, 3240(0277), 86–98.http://spiedl.org/terms

[10]. Jiang, X., Gong, M., Li, H., Zhang, M., & Li, J. (2018). A two-phase multiobjective sparse unmixing approach for hyperspectral data. IEEE Transactions on Geoscience and Remote Sensing, 56(1), 508–523. https://doi.org/10.1109/TGRS.2017.2751060

[11]. J. Li, J. M. Bioucas-Dias, A. Plaza and L. Liu, "Robust Collaborative Nonnegative Matrix Factorization for Hyperspectral Unmixing," in IEEE Transactions on Geoscience and Remote Sensing, vol. 54, no. 10, pp. 6076-6090, Oct. 2016, doi: 10.1109/TGRS.2016.2580702.

[12]. N. Keshava and J. F. Mustard, "Spectral unmixing," in IEEE Signal Processing Magazine, vol. 19, no. 1, pp. 44-57, Jan. 2002, doi: 10.1109/79.974727.

[13]. M. Iordache, J. M. Bioucas-Dias and A. Plaza, "Sparse Unmixing of Hyperspectral Data," in IEEE Transactions on Geoscience and Remote Sensing, vol. 49, no. 6, pp. 2014-2039, June 2011, doi: 10.1109/TGRS.2010.2098413.

[14]. Li, J., Li, H., Liu, Y., & Gong, M. (2021). Multi-fidelity evolutionary multitasking optimization for hyperspectral endmember extraction. Applied Soft Computing, 111, 107713. https://doi.org/10.1016/j.asoc.2021.107713

[15]. Liu, S., Bruzzone, L., Bovolo, F., & Du, P. (2016). Unsupervised multitemporal spectral unmixing for detecting multiple changes in hyperspectral images. IEEE Transactions on Geoscience and Remote Sensing, 54(5), 2733– 2748. https://doi.org/10.1109/TGRS.2015.2505183

[16]. Luo, W., Gao, L., Plaza, A., Marinoni, A., Yang, B., Zhong, L., Gamba, P., & Zhang, B. (2016). A New Algorithm for Bilinear Spectral Unmixing of Hyperspectral Images Using Particle Swarm Optimization. IEEE Journal of Selected Topics in Applied Earth Observations and Remote Sensing, 9(12), 5776–5790. https://doi.org/10.1109/JSTARS.2016.2602882

[17]. Nielsen, A. A. (2007). The regularized iteratively reweighted MAD method for change detection in multi- and hyperspectral data. IEEE Transactions on Image Processing, 16(2), 463–478. https://doi.org/10.1109/TIP.2006.888195

[18]. Pauca, V. P., Piper, J., &Plemmons, R. J. (2006). Nonnegative matrix factorization for spectral data analysis. Linear Algebra and Its Applications, 416(1), 29–47. https://doi.org/10.1016/j.laa.2005.06.025

[19]. Rajakumar, B. R. (2012). The Lion's Algorithm: A New Nature-Inspired Search Algorithm. Procedia Technology, 6, 126–135. https://doi.org/10.1016/j.protcy.2012.10.016

[20]. Rajakumar, B. R. (2014). Lion algorithm for standard and large scale bilinear system identification: A global optimization based on Lion's social behavior. Proceedings of the 2014 IEEE Congress on Evolutionary Computation, CEC 2014, 2(1), 2116–2123. https://doi.org/10.1109/CEC.2014.6900561

[21]. Schmidt, F., Schmidt, A., Tréguier, E., Guiheneuf, M., Moussaoui, S., &Dobigeon, N. (2010). Implementation strategies for hyperspectral unmixing using Bayesian source separation. IEEE Transactions on Geoscience and Remote Sensing, 48(11), 4003–4013. https://doi.org/10.1109/TGRS.2010.2062190

[22]. Uezato, T., Fauvel, M., &Dobigeon, N. (2018). Hyperspectral Image Unmixing with LiDAR Data-Aided Spatial Regularization. IEEE Transactions on Geoscience and Remote Sensing, 56(7), 4098–4108. https://doi.org/10.1109/TGRS.2018.2823419

[23]. Wang, D., Shi, Z., & Cui, X. (2018). Robust Sparse Unmixing for Hyperspectral Imagery. IEEE Transactions on Geoscience and Remote Sensing, 56(3), 1348–1359. https://doi.org/10.1109/TGRS.2017.2761912

[24]. Wang, L., Feng, Y., Gao, Y., Wang, Z., & He, M. (2018). Compressed Sensing Reconstruction of Hyperspectral Images Based on Spectral Unmixing. IEEE Journal of Selected Topics in Applied Earth Observations and Remote Sensing, 11(4), 1266–1284. https://doi.org/10.1109/JSTARS.2017.2787483

[25]. Wang, R., Li, H. C., Liao, W., Huang, X., & Philips, W. (2017). Centralized Collaborative Sparse Unmixing for Hyperspectral Images. IEEE Journal of Selected Topics in Applied Earth Observations and Remote Sensing, 10(5), 1949–1962. https://doi.org/10.1109/JSTARS.2017.2651063

[26]. Wang, Z., Wei, J., Li, J., Li, P., &Xie, F. (2021). Evolutionary multiobjective optimization with endmember priori strategy

ISSN: 1992-8645 www.jatit.org E-ISSN: 1817-3195
for large-scale hyperspectral sparse unmixing. Electronics (Switzerland), 10(17), 1–13. https://doi.org/10.3390/electronics10172079

[27]. Xu, X., Pan, B., Chen, Z., Shi, Z., & Li, T. (2021). Simultaneously Multiobjective Sparse Unmixing and Library Pruning for Hyperspectral Imagery. IEEE Transactions on Geoscience and Remote Sensing, 59(4), 3383–3395. https://doi.org/10.1109/TGRS.2020.3016941

[28]. Xu, X., & Shi, Z. (2017). Multi-objective based spectral unmixing for hyperspectral images. ISPRS Journal of Photogrammetry and Remote Sensing, 124, 54–69. https://doi.org/10.1016/j.isprsjprs.2016.12.010

[29]. Zhang, S., Li, J., Wu, Z., & Plaza, A. (2018). Spatial Discontinuity-Weighted Sparse Unmixing of Hyperspectral Images. IEEE Transactions on Geoscience and Remote Sensing, 56(10), 5767–5779. https://doi.org/10.1109/TGRS.2018.2825457